Mechanism and Machine Theory 162 (2021) 104338

Contents lists available at ScienceDirect

Mechanism and Machine Theory

journal homepage: www.elsevier.com/locate/mechmachtheory

Identification of short-wavelength contact wire irregularities in electrified railway pantograph–catenary system

Yang Song*, Anders Rønnquist, Tengjiao Jiang, Petter Nåvik

Department of Structural Engineering, Norwegian University of Science and Technology, Richard Birkelands vei 1A, Trondheim 7491, Norway

ARTICLE INFO

Article history:
Received 25 February 2021
Accepted 17 March 2021
Available online 29 March 2021

Keywords:
Railway
Pantograph–catenary interaction
Contact force
Irregularity
Ensemble empirical mode

ABSTRACT

The effect of two common types of short-wavelength irregularities (local imperfections and periodic short-wavelength irregularities) of the railway catenary on the pantograph–catenary interaction performance are studied and their potential identification approaches are explored in this paper. The analysis of the intrinsic mode functions of panhead acceleration indicates that the effect of local imperfection can be reflected in the high-order deformation mode of the contact wire. The cut-off frequency is suggested to cover the wavelength smaller than 1/8 of the dropper to dropper distance, which can be used to identify the local imperfection. The instantaneous energy obtained by the Hilbert transform is used to localise the local imperfection. The effect of periodic short-wavelength irregularities can be recognised as the introduction of non-Gaussian behaviour in the contact force at specific wavelengths. Thus, spectral kurtosis is utilised to identify the deviating wavelength. The short-wavelength irregularity can be localised by the time-frequency analysis of the intrinsic mode function containing the identified deviating wavelength. The examples with measurement data indicate the validation of the present methods with some improvements to the current equipment.

1. Introduction

Pantograph–catenary systems are widely used in the modern electrified railway to power the electric train via the sliding contact between the registration strip of the pantograph and the contact wire of the catenary, as shown in Fig. 1. The contact quality of pantograph–catenary is of great importance as it directly determines the reliability and safety of electric transmission [1]. Generally, the catenary suffers long-term impacts from the pantographs and various disturbances from environmental conditions. These factors, together with mounting imprecisions and inadequate maintenance, present the primary source of contact wire irregularity (CWI), which is the common early fault in the catenary and directly affects the interaction performance between the pantograph collector and the contact wire.

* Corresponding author.
E-mail addresses: anders.ronnquist@ntnu.no (A. Rønnquist), tengjiao.jiang@ntnu.no (T. Jiang), petter.r.navik@ntnu.no (P. Nåvik).

https://doi.org/10.1016/j.mechmachtheory.2021.104338

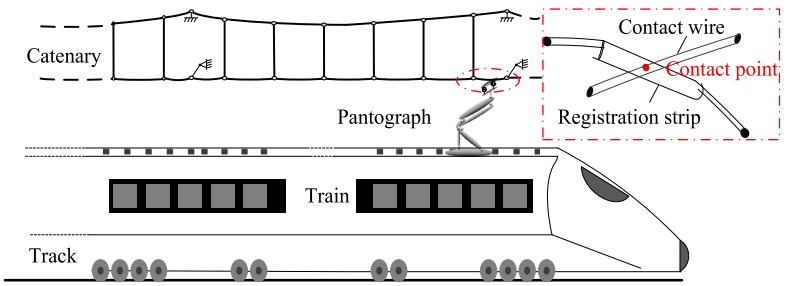

Fig. 1. Schematic of a pantograph-catenary system.

1.1. Problem description

Generally, CWIs can be divided into three types. The first is the geometrical distortion, as shown in Fig. 2(a), which is normally caused by the deformation of messenger, contact and dropper wires. The second one is the periodic short-wavelength CWI (PSW-CWI) caused by wear and manufacturing defect in the contact wire as shown in Fig. 2(b). The last one is the local imperfection caused by the wire kinks as shown in Fig. 2(c). The first type of CWI has a long wavelength and mainly affects the low-frequency performance of pantograph–catenary interaction. In contrast, the second and third ones present the main source of short-wavelength disturbance to the pantograph–catenary interaction, which directly causes hard-spot and contact loss. The CWIs are desired to identify and correct before they develop into severe faults and result in catastrophic consequences. The current standard [2] specifies that main statistics (such as the mean value, maximum value and standard deviation) of the contact force of pantograph-catenary can be used to assess the contact quality. The previous researches [3] indicate that the contact force filtered at 0–20 Hz can reflect the geometrical deformation of the catenary. Apart from the conventional dynamic inspection, some railway operators also use diesel train to regularly monitor the variation of the contact wire height. But the effect of the short-wavelength irregularities is not distinct in the time-history of contact force or the contact wire height and challenging to be identified by the regular inspection [4].

1.2. Literature review

The study of the pantograph–catenary interaction has attracted ever-increasing interest from both the scientific community and the industry, as it has been recognised as the most vulnerable part of the traction power system [5,6]. Due to the considerable expense of field experiment, various types of mathematical models of catenary were developed based on the mode superposition [7], the finite element method [8–10] and the analytical expression [11,12]. The pantograph was normally assumed as a lumped mass model which could describe several critical modes of real one [13]. The modelling of 3D pantograph has been state-of-the-art, as it can fully describe the real configuration, which is essential for the optimisation of parameters [14], the inclusion of spatial vehicle vibration [15] and the development of controllers [16,17]. The pantograph–catenary system works under complex service conditions resultant from the high-speed airflow, wind loads, temperature variations, snow and ice coating, electromagnetic forces, vehicle excitations, catenary defects and anomalies. The mathematical descriptions of these factors' effect on pantograph–catenary interaction have been developed by many researchers. The aerodynamic forces applied to the pantograph and their impact on the contact force were evaluated by Pombo et al. [18]. Different from the traditional vortex-induced vibration [19,20], the wind load normally causes the buffeting of the catenary and affects its interaction with pantographs, which was investigated in [21,22]. The aerodynamic instability of the catenary in extreme conditions was also investigated in [23]. The locomotive excitation responses evaluated by vehicle-track interaction simulation [24] and experimental test [25] were introduced to evaluate their influence on pantograph–catenary interaction performance [26]. The multiple pantograph interaction with a high-speed catenary was

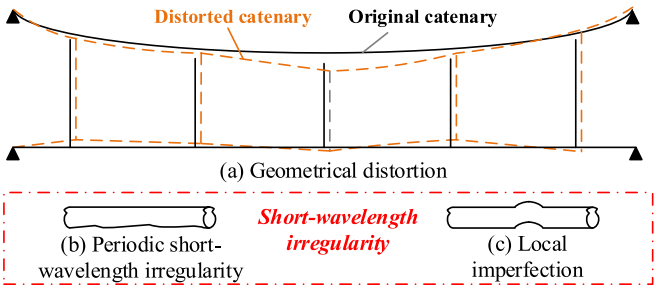

Fig. 2. Three types of contact wire irregularity.

analysed by Xu et al. [27] and Liu et al. [28], and two formulas for the optimal pantograph interval were proposed. The real anomalies of the catenary, including the defective dropper [29] and tension loss [30] were added in the assessment of the pantograph–catenary interaction. For the perspective of accident prevention, some researchers devoted their attention to the improvement of monitoring and detection technique for the pantograph–catenary system. Except using the contact force, Nåvik et al. [31] proposed an acceleration-based index to identify the pantograph fault. Jiang et al. [32] proposed a robust line-tracking photogrammetry method for monitoring the uplift of contact wire in complex backgrounds. Liu et al. [33] developed a detection method for structure parameters of the catenary cantilever using 3D point cloud data.

The effect of long-wavelength CWI and its detection technique has been widely studied and reported in exiting literature. Song et al. [34] proposed a TCUD (Target Configuration Under Dead Loads)-based method to model the catenary with realistic CWIs, and investigated the stochastic effect of contact wire height variation on the contact force [3]. Wang et al. [4] presented a time-frequency representation (TFR) to identify and localise CWIs from the contact force based on the Zhao–Atlas–Marks distribution. As for the short-wavelength CWI, the following works deserves to be mentioned.

The first one was performed by Wang et al. [35]. The real contact wire wear was included in the numerical simulation to evaluate the interaction performance of the pantograph–catenary. The results indicated that the standard deviation of low-frequency contact force was not significantly changed by the slight wear, which pointed out that the traditional assessment indicators might be invalid to evaluate the contribution of the short-wavelength CWI. The second [36] proposed the concept of catenary structural wavelength (CSW) to quantify the contribution of CWIs to interaction performance. The CSW was defined according to the catenary geometry (including the span length, half span length and dropper interval). The effect of CWIs could be extracted by removing the CSW from the measured acceleration or contact force using ensemble empirical mode decomposition (EEMD). However, it is difficult to define a CSW in actual operation for the following three reasons. Firstly, the catenary modes are dependent on the geometrical information and the deformation of the tensioned wires [37]. It is insufficient to only include the geometrical structural wavelengths (namely the dropper interval and span length) in the CSW without deformation modes. Secondly, there is an inherent variation of the catenary geometry in actual operation, which results in a wide-band structural wavelength and poses a challenge to define the CSW. Thirdly, the CWI may have the same wavelength as the contact force since most short-wavelength CWIs are the direct consequence of the contact force's long-term impact. The contribution of CWIs cannot be evaluated by merely removing the CSW from the measurement signal. In [38], the high-frequency acceleration of the pantograph head was utilised to identify the local imperfection employing RMS (Root Mean Square). In this work, the acceleration signal was measured at up to 200 Hz using a sensitive accelerometer. This solution may not be suitable for all the countries, as most railway operators only measure the dynamic parameters (e.g. stagger, contact force, acceleration and height) with a sparse distance step (e.g. 0.5 m for most countries like China, Norway and the UK). Therefore, the current issue is whether it is possible to make the best use of the current sparse measurement data to identify the local imperfection. Another problem is that the RMS is not reliable to detect the imperfection, and more sensitive indices should be investigated.

1.3. Scope and contribution

As shown in the above literature review, the local imperfection can be identified through the panhead acceleration with extremely high cut-off frequencies. If a high cut-off frequency cannot be reached, the effectiveness of the existing identification method for the short-wavelength irregularity should be re-evaluated. The main objective of this work is to study potential identification methods for the short-wavelength irregularities and the local imperfection from the measurement contact force and panhead acceleration respectively. The scope and contribution can be summarised as follows:

1) Explore the possibility to identify the local imperfection from the panhead acceleration with limited cut-off frequency, and investigate a sensitive index better to represent the local imperfection from the pantograph head acceleration.
2) Evaluate the effect of PSW-CWI on the contact force, and seek a valid index to represent the contribution of CWI with a specific wavelength.

To achieve the main goals, this paper presents a mathematical model of the pantograph–catenary interaction based on the absolute coordinate nodal formulation (ANCF), which has been proven to be an effective method to describe the geometrical nonlinearity in railway dynamics [39]. The short-wavelength CWI is properly included in the catenary model. EEMD is utilised to analyse the implication of short-wavelength CWI in each IMF. Addressing the feature of each type of short-wavelength CWI, the potential solutions are discussed. For the local imperfection, the minimum cut-off frequency of the pantograph head acceleration which can reflect the effect of local imperfection is investigated. The Hilbert spectrum is utilised to identify and localise the local imperfection. For the PSW-CWI, the spectral kurtosis [40] is adopted to indicate the non-Gaussian behaviour of contact force with a specific wavelength caused by the PSW-CWI. The time-frequency analysis is performed to localise the PSW-CWI from the corresponding IMF containing the identified deviating wavelength. Using both numerical and measurement data, the validations of the proposed identification approaches for two types of short-wavelength CWI are verified.

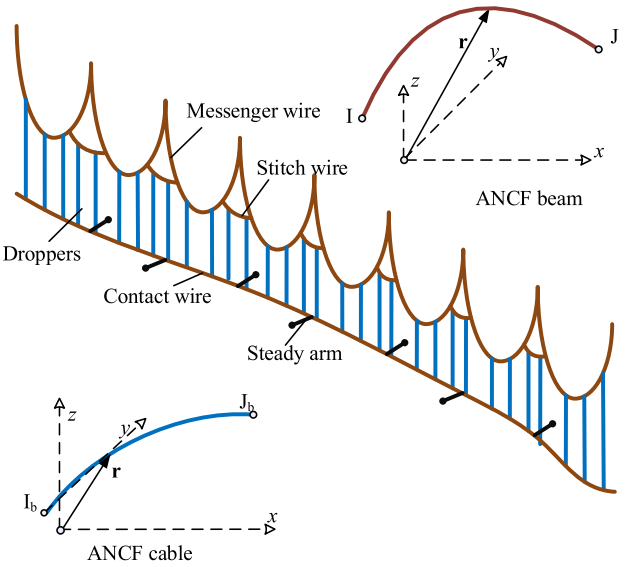

Fig. 3. Catenary model based on ANCF beam and cable elements.

1.4. Paper organization

The outline of this paper is as follows. A background description and literature review are given in Section 1. The mathematical model of the pantograph–catenary system to generate the data for subsequent analyses is described in Section 2. Section 3 discusses the potential solutions for the two types of short-wavelength CWI. The identification approach for local imperfection is proposed in Section 4 with applications to both numerical and measurement data. Section 5 presents the identification approach for PSW-CWI. Section 6 concludes this paper.

2. Numerical modelling of pantograph–catenary

In this section, a mathematical model of the pantograph–catenary system is built to generate numerical data for subsequent analyses. The catenary is modelled by ANCF. The TCUD method presented in [41] is employed to calculate the initial configuration of the catenary. The pantograph is considered as a lumped mass model. The validation of the present model is verified according to the benchmark [42] and the measurement data is collected from the Norwegian rail network.

2.1. Finite element model of catenary

The ANCF is a nonlinear finite element approach to describe the geometrical nonlinearity of large deformation. As shown in Fig. 3, the ANCF beam element is utilised to model the tensioned wires (including contact wire, messenger wire and stitch wire). The ANCF cable element is adopted to model the dropper wire. The steady arm is modelled by the truss element. The claws and clamps on the wire are assumed as lumped masses. For an ANCF beam element, the nodal degree of freedom (DOF) vector that contains the displacements and the gradients are defined as:

$$\mathbf{e} = \left[x_i \quad y_i \quad z_i \quad \frac{\partial x_i}{\partial \chi} \quad \frac{\partial y_i}{\partial \chi} \quad \frac{\partial z_i}{\partial \chi} \quad x_j \quad y_j \quad z_j \quad \frac{\partial x_j}{\partial \chi} \quad \frac{\partial y_j}{\partial \chi} \quad \frac{\partial z_j}{\partial \chi} \right]^{\mathrm{T}} \tag{1}$$

in which, χ is the local coordinate in the undeformed configuration ranging from 0 to the element length L_0. The position vector in the deformed configuration $\mathbf{r}$ is interpolated using the shape function matrix $\mathbf{S}$ as

$$\mathbf{r} = \mathbf{S}\mathbf{e} \tag{2}$$

$\mathbf{S}$ can be defined as follows:

$$\mathbf{S} = \begin{bmatrix} S_1 & & & S_2 & & & S_3 & & & S_4 & & \\ & S_1 & & & S_2 & & & S_3 & & & S_4 & \\ & & S_1 & & & S_2 & & & S_3 & & & S_4 \end{bmatrix}$$

$$\begin{aligned} S_1(\xi) &= 1 - 3\xi^2 + 2\xi^3 \\ S_2(\xi) &= l_0\left(\xi + \xi^3 - 2\xi^2\right) \\ S_3(\xi) &= 3\xi^2 - 2\xi^3 \\ S_4(\xi) &= l_0\left(\xi^3 - \xi^2\right) \end{aligned} \tag{3}$$

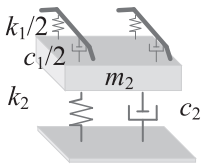

Fig. 4. Lumped mass model of pantograph with flexible collectors.

The strain energy obtained from the contribution of axial and bending deformation is expressed by

$$U = \frac{1}{2}\int_0^{L_0} \left(EA\varepsilon_l^2 + EI\kappa^2\right) d\chi \tag{4}$$

in which, E is Young's modulus, A is the section area, I is the moment inertial of the wire, ε_l is the longitudinal strain and κ is the curvature. The generalised elastic forces can be defined as

$$\mathbf{Q} = \left(\frac{\partial U}{\partial \mathbf{e}}\right)^T = \mathbf{K}_\mathrm{e}\mathbf{e} \tag{5}$$

In this way, the element stiffness matrix $\mathbf{K}_\mathrm{e}$ is obtained. In the shape-finding procedure, the tangent stiffness matrix is used to calculate the incremental nodal DOF vector $\Delta\mathbf{e}$ and the incremental unstrained length ΔL_0. The corresponding tangent stiffness matrices $\mathbf{K}_\mathrm{T}$ and $\mathbf{K}_\mathrm{L}$ can be obtained as follows:

$$\Delta\mathbf{F} = \frac{\partial \mathbf{Q}}{\partial \mathbf{e}}\Delta\mathbf{e} + \frac{\partial \mathbf{Q}}{\partial L_0}\Delta L_0 = \mathbf{K}_\mathrm{T}\Delta\mathbf{e} + \mathbf{K}_\mathrm{L}\Delta L_0 \tag{6}$$

Similarly, the tangent stiffness matrices of the ANCF cable element can also be derived. It should be noted that the cable element used to model the dropper can only withstand tension but not compression. The axial stiffness changes to zero when the dropper works in compression. Assembling the element matrices yields the global incremental equilibrium equation for the whole catenary as follows:

$$\Delta\mathbf{F}^\mathrm{G} = \mathbf{K}_\mathrm{T}^\mathrm{G}\Delta\mathbf{U}_\mathrm{C} + \mathbf{K}_\mathrm{L}^\mathrm{G}\Delta\mathbf{L}_0 \tag{7}$$

where $\Delta\mathbf{F}^\mathrm{G}$ is the global unbalanced force vector. $\mathbf{K}_\mathrm{T}^\mathrm{G}$ and $\mathbf{K}_\mathrm{L}^\mathrm{G}$ are the global stiffness matrices related to the incremental nodal displacement vector $\Delta\mathbf{U}_\mathrm{C}$ and the incremental unstrained length vector $\Delta\mathbf{L}_0$, respectively. It is seen that $[\mathbf{K}_\mathrm{T}^\mathrm{G} \quad \mathbf{K}_\mathrm{L}^\mathrm{G}]$ is not a square matrix. The total number of unknowns in Eq. (7) exceeds the total number of equations, which leads to undetermined solutions. Hence, additional constraint conditions are provided to suppress undesired movements, according to the design specifications. Thus, the following additional constraint conditions are defined.

- The vertical positions of the dropper point in the contact wire are restricted to describe the reserved pre-sag.
- The longitudinal direction of each node is restricted to suppress the longitudinal movement.
- The tensions are applied to stitch wires and the endpoints of messenger and contact wires.

With the help of the above three types of constraints, $[\mathbf{K}_\mathrm{T}^\mathrm{G} \quad \mathbf{K}_\mathrm{L}^\mathrm{G}]$ is reduced to a square matrix. The strained and unstrained lengths of all the elements can be calculated by solving Eq. (7). In this way, the initial configuration of the catenary is determined. Introducing a consistent mass matrix and Rayleigh damping, the equation of motion for the catenary system is written by

$$\mathbf{M}_\mathrm{C}^\mathrm{G}\ddot{\mathbf{U}}_\mathrm{C}(t) + \mathbf{C}_\mathrm{C}^\mathrm{G}\dot{\mathbf{U}}_\mathrm{C}(t) + \mathbf{K}_\mathrm{C}^\mathrm{G}(t)\mathbf{U}_\mathrm{C}(t) = \mathbf{F}_\mathrm{C}^\mathrm{G}(t) \tag{8}$$

2.2. Pantograph model

The pantograph is modelled as a lumped mass model with flexible collectors as shown in Fig. 4. Each collector is discretized into several Euler-Bernoulli beam elements. The mass of the pantograph head is evenly distributed along the collector. Generally, the collector is made of two types of materials, namely Graphite and Aluminium. The bending stiffness of the collector is calculated based on the mixture theory [43]. Apart from the pantograph aerodynamics [44,45], the flexibility of the framework does not have a significant contribution to the response within the frequency range of interest in this work. Therefore, the pantograph framework is treated as a lumped mass here. A penalty function method is utilised to couple the two systems. Based on the assumption of the relative penetration generated between the two contact surfaces, the contact force f_c can be calculated by:

$$f_\mathrm{c} = \begin{cases} k_\mathrm{s}\delta & if\ \delta > 0 \\ 0 & if\ \delta \le 0 \end{cases} \tag{9}$$

in which, the penetration δ can be evaluated by

$$\delta = z_\mathrm{p} - z_\mathrm{c} - z_\mathrm{ir} \tag{10}$$

Table 1
Static validation of the present model against benchmark.

Dropper No.	Pre-sag			Elasticity		
	Benchmark (mm)	Present (mm)	Error (%)	Benchmark (mm/N)	Present (mm/N)	Error (%)
Sup	0	0	0	0.206	0.19257	6.52
1	0	0	0	0.165	0.15647	5.17
2	24	24	0	0.273	0.26774	1.93
3	41	41	0	0.345	0.3268	5.28
4	52	52	0	0.388	0.36832	5.07
5	55	55	0	0.4	0.37509	6.23
6	52	52	0	0.388	0.36832	5.07
7	41	41	0	0.345	0.3268	5.28
8	24	24	0	0.273	0.26774	1.93
9	0	0	0	0.165	0.15647	5.17
Sup	0	0	0	0.206	0.19257	6.52

Table 2
Dynamic validation of the present model against benchmark.

	Benchmark	Present model	Error
Mean [N]	169	169.15	0.09%
Std. (0–20 Hz) [N]	53.91	52.59	2.45%
Std. ed. (0–2 Hz) [N]	38.27	38.25	0.05%
tStd. d. (0–5 Hz) [N]	41.04	41.00	0.10%
(Std. 5–20 Hz) [N]	34.80	32.99	5.20%
Max. [N]	313.22	305.85	2.35%
Min. [N]	60.40	56.22	6.9%

where z_p, z_c and z_{ir} are the vertical displacements of the pantograph head, the contact wire and the irregularity. Using Eq. (9), the equation of motion for the pantograph–catenary system can be written by

$$\mathbf{M}^G\ddot{\mathbf{U}}(t) + \mathbf{C}^G\dot{\mathbf{U}}(t) + \mathbf{K}^G(t)\mathbf{U}(t) = \mathbf{F}^G(t) \tag{11}$$

in which $\mathbf{M}^G$, $\mathbf{C}^G$ and $\mathbf{K}^G(t)$ are the mass, damping and stiffness matrices for the whole system, respectively. $\mathbf{F}^G(t)$ is the external force vector. A Newmark integration scheme is adopted to solve Eq. (11). The stiffness matrix $\mathbf{K}^G(t)$ is updated according to the catenary deformation in each time step to fully describe the geometrical nonlinearity and the slackness of droppers.

2.3. Model validation

Two numerical simulations are presented to validate the present model of pantograph–catenary interaction. The first one is to use the reference model in the benchmark [42] and compare the results with the mean values of the results obtained by ten mainstream software. The second one is to use the design data in the Norwegian network to model a realistic pantograph-catenary system and compare the results with the measurement data collected by a regular inspection vehicle.

The benchmark provides the results for both static and dynamic validations [46]. In the static validation, the pre-sag and elasticity of the contact wire obtained by the present model are compared with the benchmark in Table 1. It shows that the pre-sag obtained by the present method is exactly the same as the benchmark. The maximum error of the elasticity is just 6.52%. The dynamic validation is implemented by comparing the key contact force statistics with the benchmark. As shown in Table 2, the results of the present model show good consistency with the benchmark. The most significant error only reaches 6.9% for the minimum contact force.

Another numerical example is implemented by comparison with the measurement data from the “Gardermobanen” rail line in Norway, going from Oslo to Eidsvoll. The property parameters of the catenary for the analysis section is presented in Table 3. The inspection vehicle regularly runs at 160 km/h. This speed is adopted in this validation and the subsequent analyses. The pantograph on the roof of an inspection train is WBL 85, of which the lumped-mass parameters can be found in Table 4. In this case, the pantograph head is modelled by two deformable collectors. The first-order natural frequency of the collector is calculated as 65 Hz, which is consistent with the experimental results in [47]. Based on the TCUD method, the initial configuration of the catenary is calculated and presented in Fig. 5. The comparison with the measurement data is presented in Table 5. It is seen that the maximum error of the simulation result against the measurement data reaches 12.18%, which is still lower than the acceptance threshold of 20% specified in the standard [46].

3. Potential solutions

In this section, the potential solutions for identifying the two classic types of short-wavelength CWIs are discussed based on the simulation results. The local imperfection with 2 mm amplitude is added to the position of 620 m in the contact

Table 3
Catenary property parameters.

Total Length	1.012 km
Contact Wire Tension	15 kN
Messenger Wire Tension	15 kN
Stitch Wire Tension	2.8 kN
Contact Wire Area	120 mm^2
Messenger Wire Area	65.8 mm^2
Stitch Wire Area	3.44 mm^2
Contact Wire Linear Density	1.07 kg/m
Messenger Wire Linear Density	0.596 kg/m
Number of spans in contact with pantograph	18

Table 4
Pantograph parameters.

Mass of panhead	5.2 kg
Mass of frame	15.2 kg
Contact spring	100,000 N/m
Spring between panhead and frame	5400 N/m
Spring between frame and train roof	0 N/m
Damping between panhead and frame	40 N s/m
Damping between frame and train roof up	63.5 N s/m
Damping between frame and train roof down	63.5 N s/m
Friction between frame and train roof	7 N
Static uplift force	50 N
Aerodynamic uplift force	$0.0068v^2$

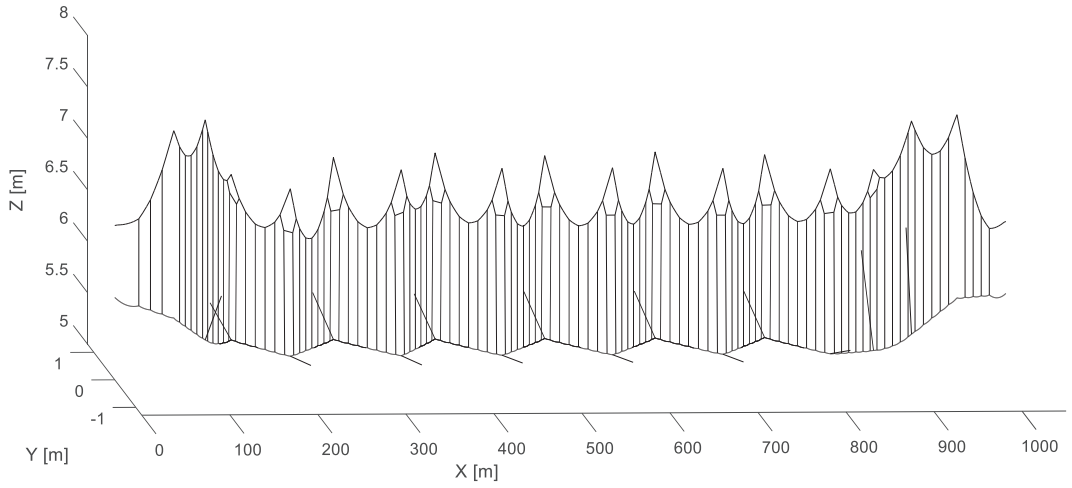

Fig. 5. Initial configuration of catenary.

wire. The PSW-CWI is represented by a sinusoidal function with a 3.3 m wavelength and 0.5 m amplitude, which is applied to the effective range from 625.9 m to 643.46 m.

3.1. Potential solution for local imperfection

The numerical simulation is performed with the abovementioned classic local imperfection in the catenary. An accelerometer is placed on the edge of each collector [38]. In this work, the acceleration of the front collector is taken as the analysis object. The resulting panhead acceleration with 200 Hz cut-off frequency is presented in Fig. 6. It is seen that the panhead acceleration experiences a significant peak when the pantograph passes the local imperfection. According to [38], the effect of local imperfection can be fully described by the panhead acceleration when the cut-off frequency reaches 200 Hz. However, most railway operators around the world do not equip the instrumented pantograph with high-sensitive accelerometers. This section investigates the potential of using low-frequency acceleration to identify the local imperfection. EEMD is a data-driven algorithm which has been used in various industrial backgrounds [48,49] to decompose a signal into several IMFs. In this work, EEMD is used to investigate the effect of local imperfection on each IMF of the acceleration signal.

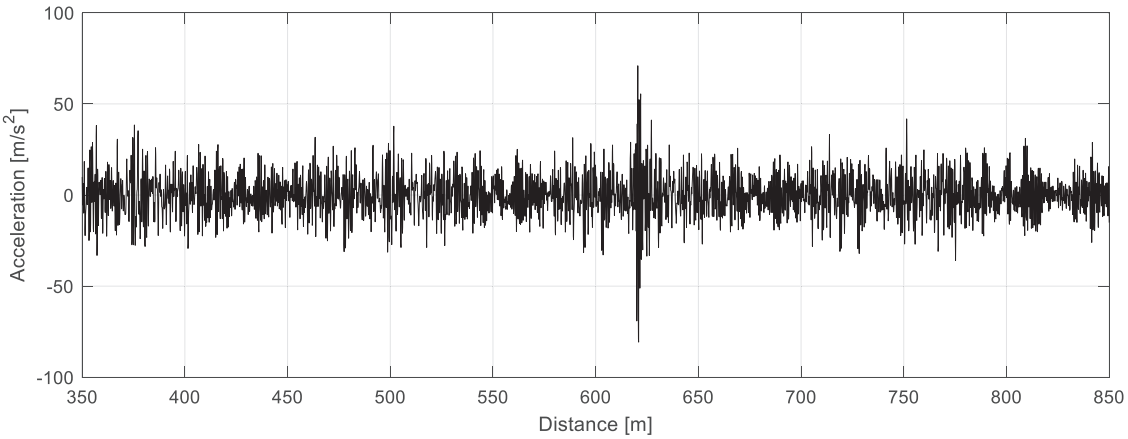

Fig. 6. Acceleration of front collector with 200 Hz cut-off frequency.

The empirical mode decomposition (EMD) can decompose a given signal $x(t)$ into a number N of IMFs $d_j(t)$, $j = 1, 2, \cdots, N$ and a residual $r(t)$ through an iterative procedure. The sum of all the IMFs and the residual precisely yields the original signal. However, mode mixing is an urgent issue for traditional EMD, which largely restricts the use of this method [50]. To resolve this problem, EEMD is proposed based on the dyadic property of EMD when dealing with white noise. EEMD utilises additional white noise to ensure the full physical meaning of the IMFs. Fig. 7 shows the IMFs of the panhead acceleration and their spectrums over the wavelength. It is seen that the effect of the local imperfection is only observed from the first three IMFs but not significant in other IMFs. The physical meaning of each IMF can be revealed by observing its spectrum. It is seen IMFs 6 and 7 in Figs. 7 (h-i) are related to the span length of the catenary. IMF 5 in Fig. 7 (f-g) denotes the dropper to dropper (DD) interval. The first four IMFs represent the deformation mode of the contact wire related to the 1/16, 1/8, 1/4 and 1/2 of DD, respectively. It is seen that the effect of the local imperfection is reflected from the mode which has a corresponding wavelength smaller than 1/4 of DD. If the cut-off frequency can cover the wavelength of 1/8 of DD, the local imperfection can be significantly reflected in the panhead acceleration. For the given case, the dropper intervals are 8–12 m, and the minimum 1/8 of DD is around 1 m. Assuming that the train speed is 160 km/h, the cut-off frequency should be improved to 45 Hz to fully cover the wavelength of 1/8 of DD. Considering the intrinsic nonlinearity of catenary and the loss of information in the filter, a higher cut-off frequency is desired in practice. The identification effectiveness is discussed in the next Section with different cut-off frequencies. It should be noted that the Norwegian railway operator implements the regular inspection vehicles with a measurement distance step of 0.5 m, which is close to the Nyquist frequency and cannot fully cover the contribution of 1/8 of DD in the real measurement. But it may have the potential to be improved to cover a part of the 1/8 of DD without a significant effort. Based on this idea, the EEMD can be used to decompose the signal and extract the IMF related to 1/8 of DD. The whole identification procedure is given in Section 4 with the application to the numerical and measurement data.

3.2. Potential solution for psw-cwi

The numerical simulations are performed with and without the abovementioned PSW-CWI. The resulting contact forces filtered within 0–20 Hz are presented in Fig. 8. It is seen that the early PSW-CWI only causes a slight disturbance to the contact force time-history. The contact force standard deviation increases by 1.04% when the PSW-CWI is introduced. The traditional indices specified in the standard [2] are not allowed to quantify the effect of PSW-CWI on the contact force. Through the frequency analysis in Fig. 9, it is seen that the PSW-CWI wavelength is the same as one of the original contact force wavelength components. The PSW-CWI only leads to a slight difference in the energy at a wavelength of 3.3 m. The

Table 5
Dynamic validation of present model against measurement data.

	Measurement	Present model	Error
Mean [N]	92.14	92.34	0.22%
Std. (0–20 Hz) [N]	11.53	10.59	8.15%
Std. (0–5 Hz) [N]	9.01	8.86	1.66%
Std. (5–20 Hz) [N]	6.33	5.72	9.64%
Max. [N]	126.64	125.44	0.95%
Min. [N]	52.85	57.14	8.12%
Range of vertical position of the point of contact [mm]	78	68.5	12.18%

method proposed in [36] is not allowed to identify this type of CWI. In this work, a new approach is proposed to solve this problem. The PSW-CWI can be regarded as a series of local sinusoidal disturbances with a specific wavelength to the contact force. The presence of such disturbance can affect the Gaussian distribution of the signal at specific frequencies. This feature can be utilised to evaluate the effect of PSW-CWI and identify the deviating wavelength. The common indicator that can indicate the non-Gaussian behaviour in the frequency domain is the spectral kurtosis (SK) [40]. The SK of a given signal can be calculated according to the following mathematical procedure.

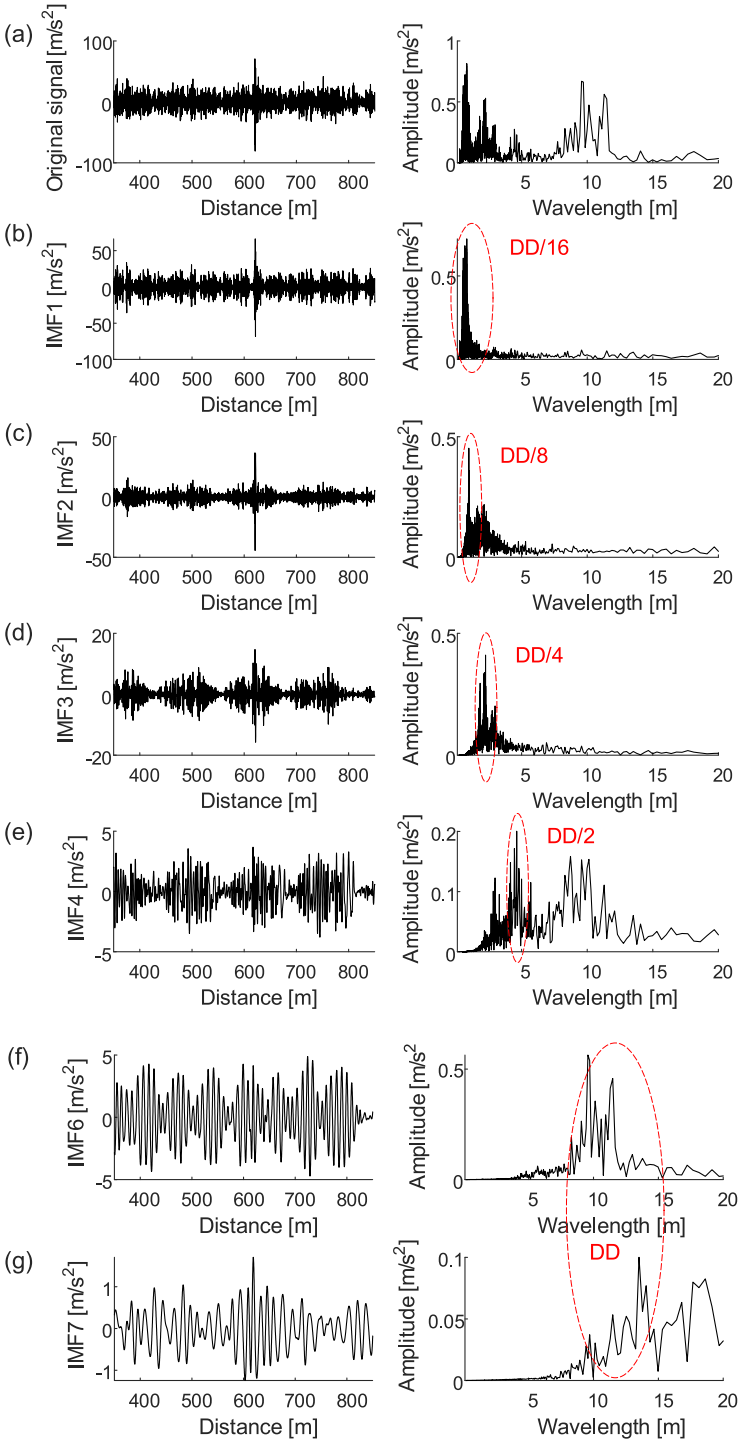

Fig. 7. IMFs of panhead acceleration and their frequency spectrums: a) original signal and its spectrum; b) IMF 1 and its spectrum; c) IMF 2 and its spectrum; d) IMF 3 and its spectrum; e) IMF 4 and its spectrum; f) IMF 5 and its spectrum; g) IMF 6 and its spectrum; h) IMF 7 and its spectrum; i) IMF 8 and its spectrum;

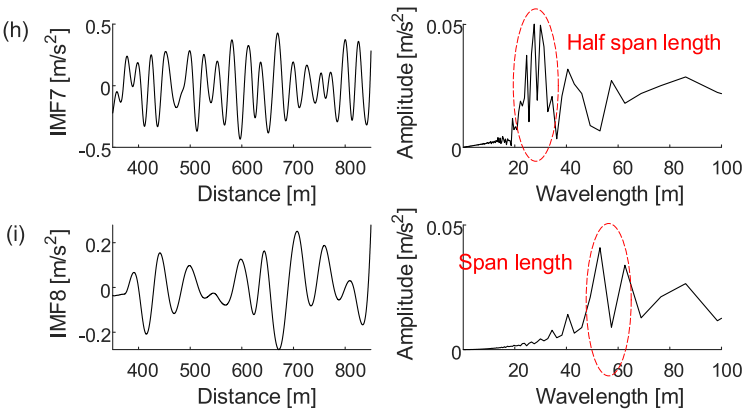

Fig. 7. Continued

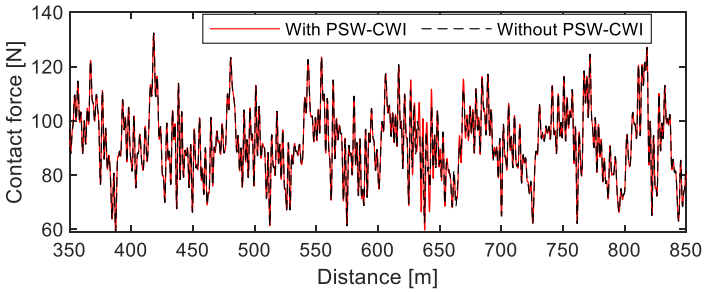

Fig. 8. Contact force with 20 Hz cut-off frequency.

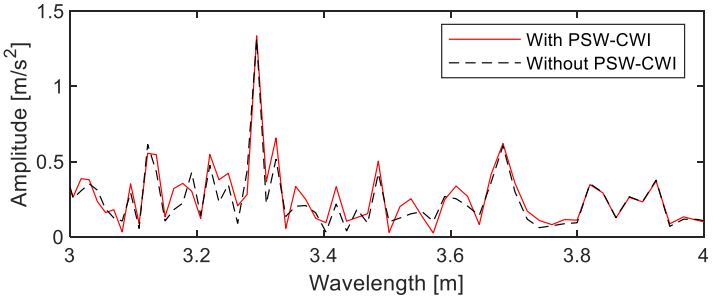

Fig. 9. Spectrum of contact force with and without PSW-CWI.

For a given signal $x(t)$, the short-time Fourier transform (STFT) $S(t, f)$ can be calculated by

$$S(t,f) = \int_{-\infty}^{+\infty} x(t) w(t-\tau) e^{-2\pi f t} \mathrm{d}t \tag{12}$$

in which, $w(t-\tau)$ is the window function used in STFT, and τ is the window length. The SK can be calculated as:

$$K(f) = \frac{\langle |S(t,f)|^4 \rangle}{\langle |S(t,f)|^2 \rangle^2} - 2, \quad f \neq 0 \tag{13}$$

where $\langle \cdot \rangle$ is the time-average operator.

Through the above procedure, the SKs of contact force with and without PSW-CWI are presented in Fig. 10. It is seen that the SK undergoes a significant increase at the wavelength of 3.3 m, which indicates that the Gaussian behaviour of the contact force at this specific wavelength deteriorates. In this way, the deviating wavelength can be determined. However, it should be noted that an SK benchmark to represent the healthy statues should be provided for the comparison. As for the measurement data, multiple inspections can be used to compare their SKs and determine the deviating wavelength. Then EEMD can be used to extract the IMF containing the deviating wavelength. The PSW-CWI can be localised by the time-frequency analysis. The whole identification procedure is given in Section 5 with the application to numerical and measurement data.

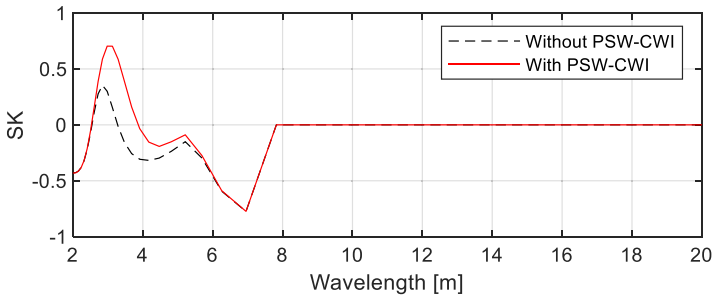

Fig. 10. Spectral kurtosis of contact force with and without PSW-CWI.

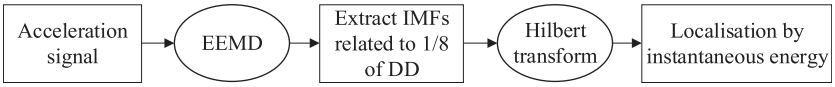

Fig. 11. Identification procedure for local impact.

4. Identification of local imperfection

Through the analysis in Section 3.1, this section proposes the identification procedure for the local imperfection using the acceleration with the cut-off frequency covering a 1/8 of DD wavelength. Then the numerical and measurement data are adopted to validate the proposed method.

4.1. Identification procedure

The identification procedure for the local imperfection from the panhead acceleration is proposed in Fig. 11. The IMF related to 1/8 of DD is extracted from the acceleration signal through the EEMD. Different to the previous mobile RMS [38], a more sensitive indicator, instantaneous energy obtained by the Hilbert transform is used here to indicate the position of local imperfection. The local imperfection is localised by searching the extremely large peak of the instantaneous energy. The mathematical procedure for the Hilbert transform is given as follows.

For a given time series $x(t)$, an analytical signal $z(t)$ can be formulated as

$$z(t) = x(t) + iy(t) \tag{14}$$

in which, i is the imaginary unit, $y(t)$ is the Hilbert transform of $x(t)$, which can be calculated by

$$y(t) = \frac{1}{\pi}\int_{-\infty}^{+\infty}\frac{x(s)}{t-s}\mathrm{d}s \tag{15}$$

In this way, the analytical signal can be re-written in the following form:

$$z(t) = a(t)e^{i\theta(t)} \tag{16}$$

in which, $a(t)$ is the instantaneous amplitude and $\theta(t)$ is the instantaneous phase. The instantaneous energy can be calculated by $|a(t)|^2$, and the instantaneous frequency is defined by $\frac{\mathrm{d}\theta(t)}{\mathrm{d}t}$.

4.2. Application to numerical results

The validation of the present identification procedure is demonstrated through several numerical simulations. The train speed in these numerical examples is set as same as the inspection vehicle speed 160 km/h. The local imperfections with different amplitudes and positions are included in the catenary to perform the numerical simulations.

1) With different cut-off frequencies

The obtained signal in Fig. 6 is adopted here to analyse the identification effectiveness and feasibility. The accelerations filtered with 40 Hz, 50 Hz, 60 Hz and 70 Hz cut-off frequencies are presented in Fig. 12. When the cut-off frequency moves up to 60 Hz, the impact of local imperfection can be significantly observed from the acceleration, which is not difficult to be identified through a traditional mobile RMS [38]. When the cut-off frequency is just over the critical value (45 Hz) to cover the wavelength of 1/8 of DD, the effect of local imperfection is not distinct in the acceleration (see Fig. 12(b)), and the mobile RMS may lose its effectiveness. The EEMD is used to decompose the acceleration, and the IMFs' related to the 1/8 of DD with different cut-off frequencies are presented in Fig. 13. The corresponding instantaneous energies are presented in Fig. 14. It is seen that the local imperfection cannot be identified when the cut-off frequency is 40 Hz, which is lower than the critical value (45 Hz) to cover the wavelength of 1/8 of

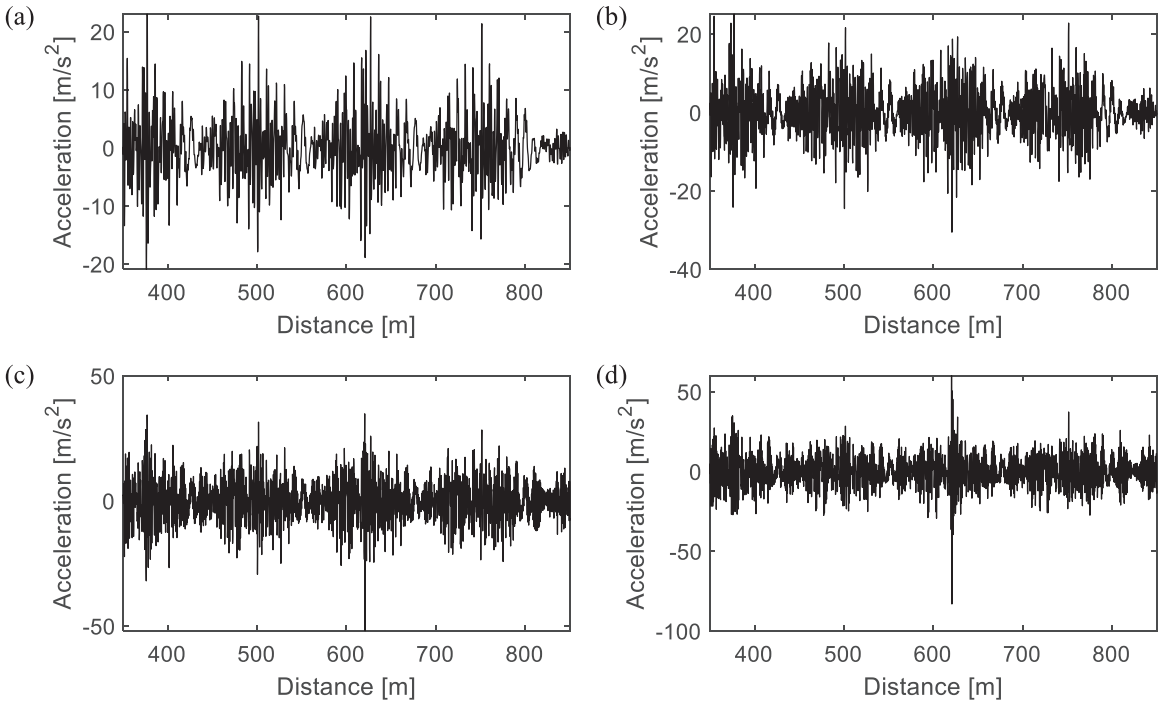

Fig. 12. Panhead accelerations with different cut-off frequencies: (a) 40 Hz; (b) 50 Hz; (c) 60 Hz; (d) 70 Hz.

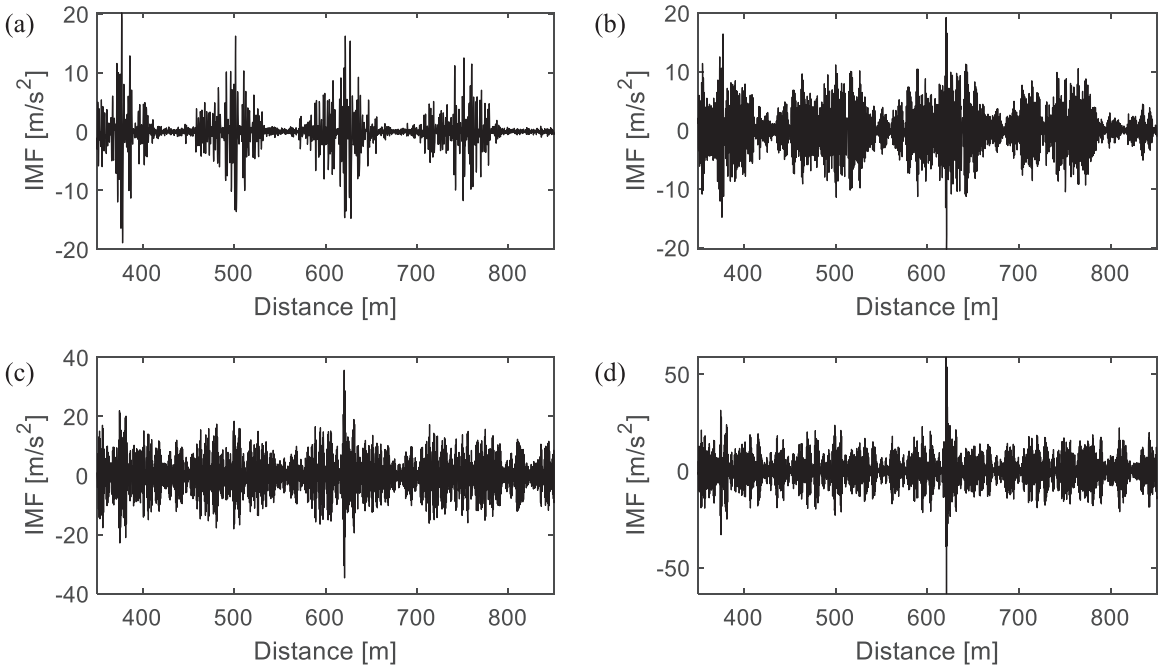

Fig. 13. IMFs related to 1/8 of DD with different cut-off frequencies: (a) 40 Hz; (b) 50 Hz; (c) 60 Hz; (d) 70 Hz.

DD. Even though the local imperfection effect cannot be distinctly seen in the panhead acceleration time-history with 50 Hz cut-off frequency, it can still be accurately identified and localised by the present method. The increase of the cut-off frequency makes the identification results more significant, which provides the feasibility to identify smaller local imperfections.

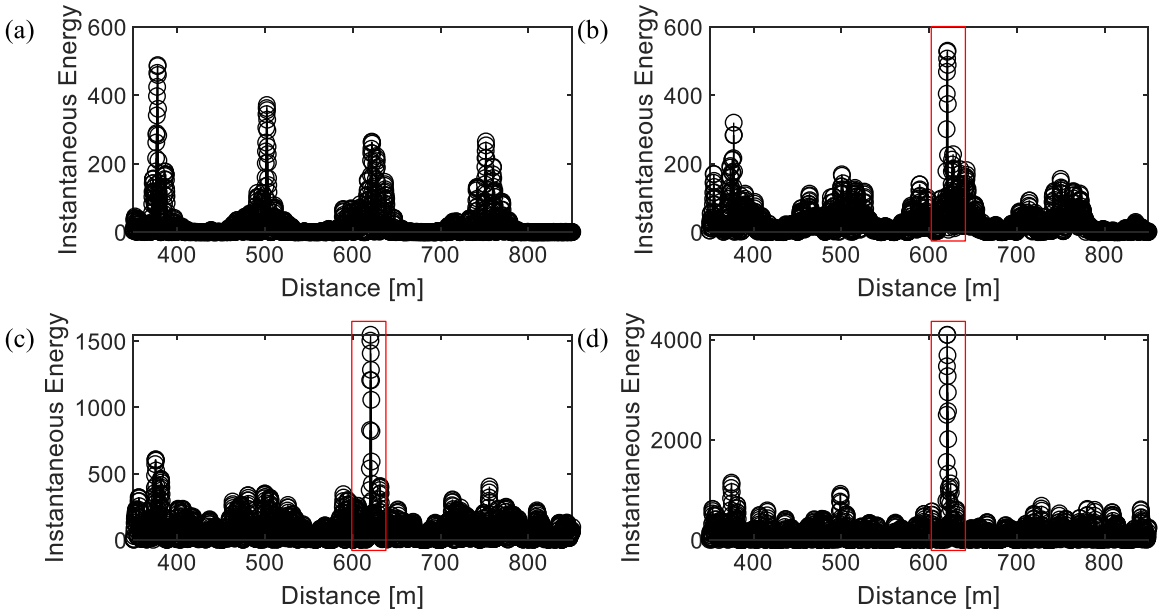

Fig. 14. Instantaneous energies of the IMF related to 1/8 of DD with different cut-off frequencies: (a) 40 Hz; (b) 50 Hz; (c) 60 Hz; (d) 70 Hz.

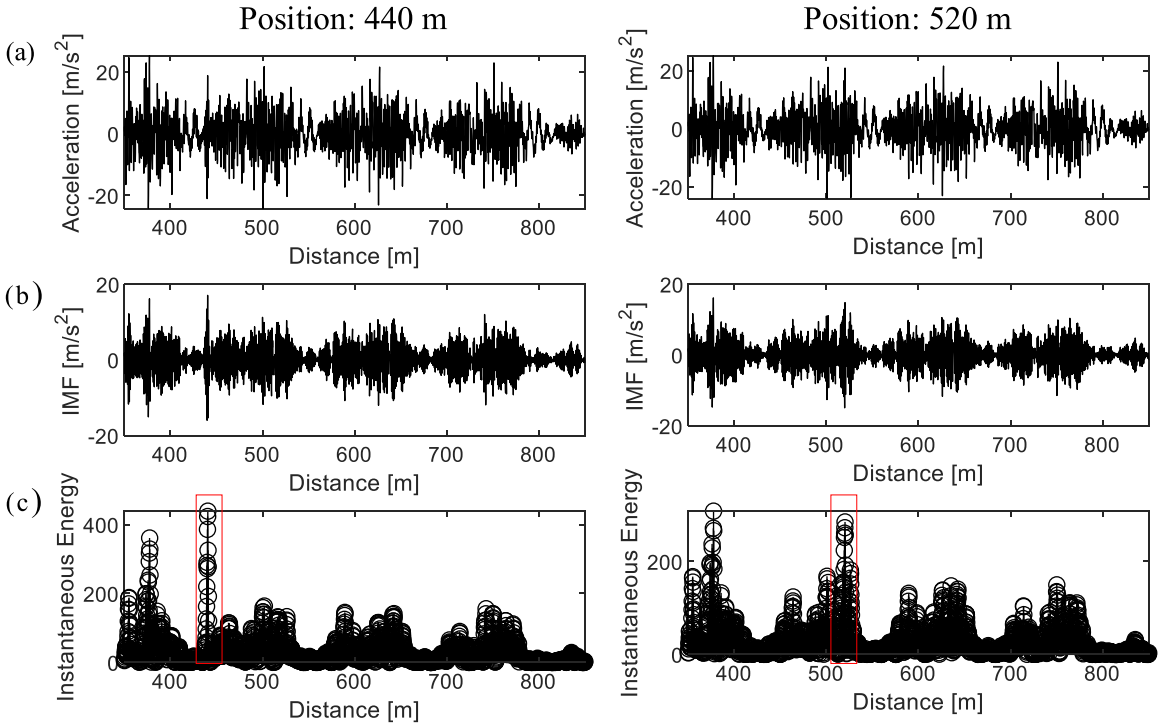

Fig. 15. Identification of local imperfection at different positions using 50 Hz cut-off frequency: (a) Panhead acceleration; (b) Extracted IMF related to 1/8 of DD; (c) Instantaneous energy.

2) With different positions

Three local imperfections are added to the positions at 440 m and 520 m in the contact wire to perform the numerical simulations. Using a 50 Hz cut-off frequency, the resulting accelerations are presented in Fig. 15(a). The corresponding IMF for each case is extracted and presented in Fig. 15(b), which is related to the 1/8 of DD wavelength component. Employing the Hilbert transform, the instantaneous energies are presented in Fig. 15(c). It is seen that some significant peaks can be observed at the positions of local imperfection. Apart from the ones caused by the local imperfection, some other peaks

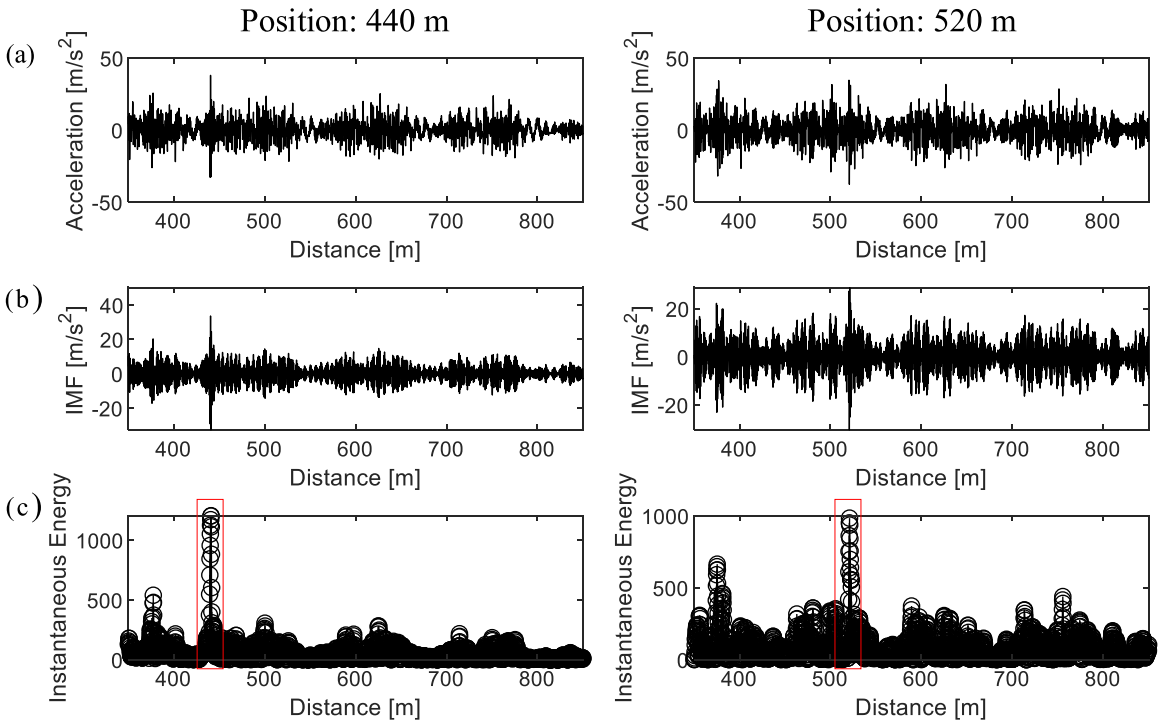

Fig. 16. Identification of local imperfection at different positions using 60 Hz cut-off freqeuncy: (a) Panhead acceleration; (b) Extracted IMF related to 1/8 of DD; (c) Instantaneous energy.

can also be observed in the instantaneous energy, which may be attributed to the implication of elasticity discontinuity, wave reflection and lumped mass in the contact wire. The best solution is to increase the cut-off frequency to cover more deformable modes. The identification results with 60 Hz cut-off frequency are presented in Fig. 16. It is seen that the identification approach provides more reliable results with a higher cut-off frequency. If the cut-off frequency cannot be reached, some potential solutions are discussed in Section 6.

4.3. Application to measurement data

The present identification procedure is implemented with the measurement panhead acceleration of two tensile sections (from 41.47 to 43.36 km) in the "Gardermobanen" railway line. The distance step for this measurement is 0.5 m. The panhead acceleration and its spectrum are presented in Fig. 17(a) and (b), respectively. It should be noticed that the measurement data are filtered with 20 Hz cut-off frequency according to the assessment standard [2], which cannot even fully describe the 1/4 of DD wavelengths. Through EEMD, the first five IMFs and their spectrums are presented in Fig. 17 (b–f). It is seen that the first one represents the intrinsic mode related to the wavelength of 1/4 of DD. Through the Hilbert transform to the first IMF, the instantaneous energy versus the distance is presented in Fig. 18. It is seen that the maximum peak of instantaneous energy appears at around 42.37 km, which is the overlap transition of the two tensile sections (according to the design specification). The variation of the contact wire height in the transition of two tensile sections presents the common local imperfection for the pantograph-catenary interaction. The smaller local imperfection, which affects the higher-order deformation mode of the contact wire cannot be identified by the low cut-off frequency. The cut-off frequency is desired to move up to cover the double sampling step, which can describe wavelengths down to 1/8 of DD and have the potential to identify smaller local imperfection.

5. Identification of PSW-CWI

According to the analysis in Section 3.2, this section proposes the identification procedure for the PSW-CWI. The numerical and measurement data are adopted to validate the proposed method.

5.1. Identification procedure

The identification procedure for the PSW-CWI from the contact force is proposed in Fig. 19. The SK of contact force is utilised to identify the deviating wavelength. Then EEMD is used to extract the IMF containing the deviating wavelength.

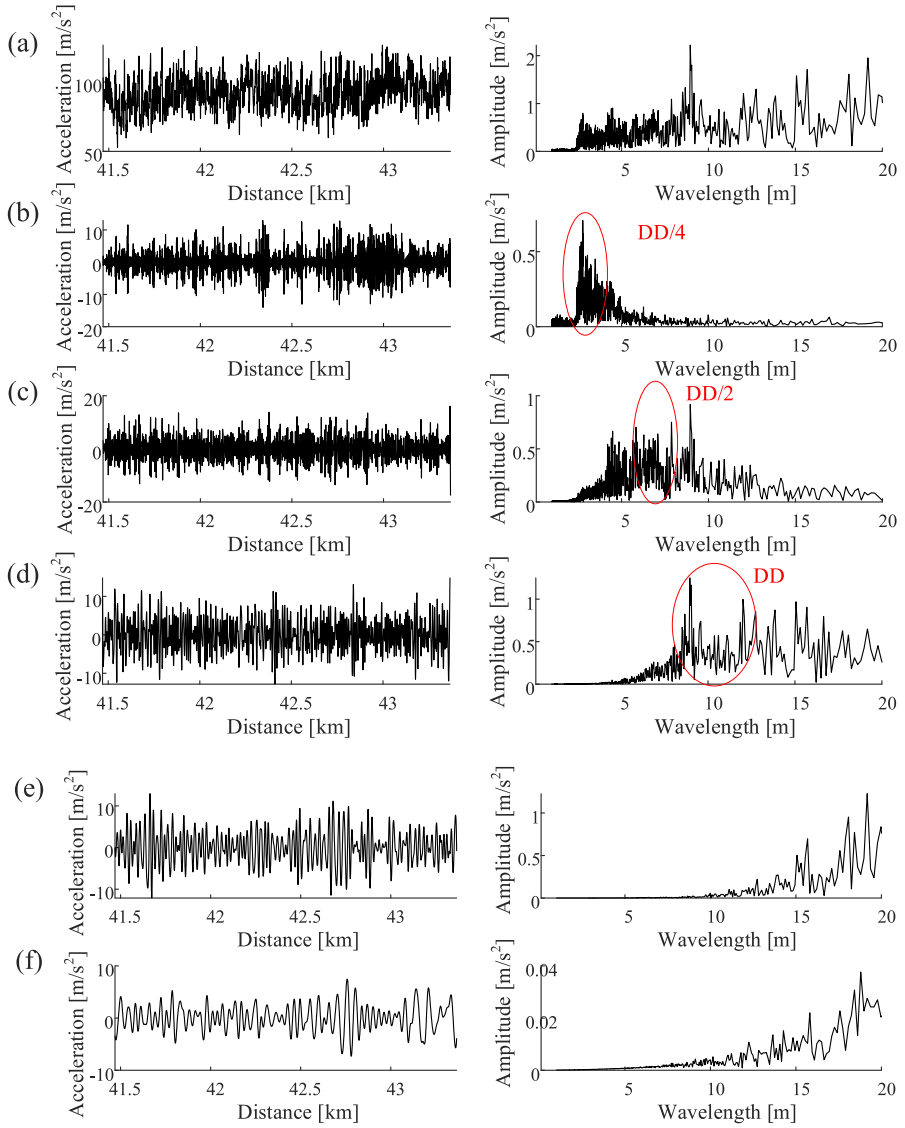

Fig. 17. (a) Original measured panhead acceleration and its spectrum; (b) IMF 1 and its spectrum; (c) IMF 2 and its spectrum; (d) IMF 3 and its spectrum; (e) IMF 4 and its spectrum; (f) IMF 5 and its spectrum.

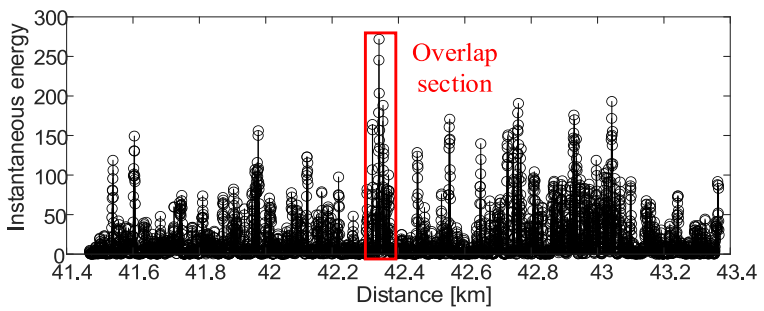

Fig. 18. Instantaneous energy of the first IMF.

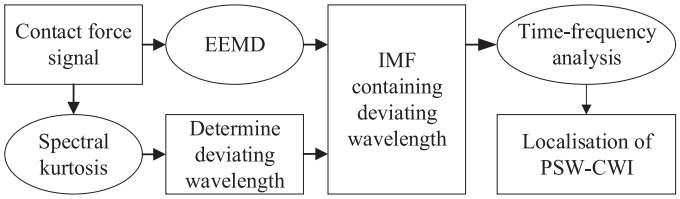

Fig. 19. Identification procedure for PSW-CWI.

The time-frequency analysis is performed to localise the PSW-CWI based on the smoothed pseudo-Wigner-Ville distribution (SPWD). The generalised quadratic TFR $C(t,\omega;\phi)$ of the corresponding IMF series $f(t)$ with the kernel $\phi(t,\nu)$ is defined as [51]

$$C(t,\omega;\phi)=\frac{1}{4\pi^2}\int\int\int\phi(t,\nu)e^{-j\omega\tau}e^{-j\nu(t-u)} f(u+\tfrac{\tau}{2})f^*(u-\tfrac{\tau}{2})\mathrm{d}u\mathrm{d}\tau\mathrm{d}\nu \tag{18}$$

where the f^* denotes complex conjugation of f. t and ω are the instantaneous time and angular frequency respectively. u, τ and ν are the running positions, time and frequency variables in the integration respectively. The quadratic TFR is obtained through a triple integral, including dual Fourier transform in time (t-u) and τ with the autocorrelation of $f(t)$. Mainly $C(t,\omega;\phi)$ describes the signal energy distribution in the time-frequency domain. When the kernel $\phi(t,\nu)=1$, $C(t,\omega;\phi)$ is a WVD (Wigner-Ville Distribution), which is the basic form of the quadratic class. According to [4], the basic form does not have an excellent performance to describe the time-frequency characteristics of contact forces, as the WVD's variants suffer from severe interference of cross-term. In this paper, the smoothed pseudo-WVD (SPWD) is employed to reduce the interference of cross-term. The kernel of this typical quadratic TFR is expressed as follows:

$$\phi(t,\nu)=\eta\left(\frac{\tau}{2}\right)\eta*\left(-\frac{\tau}{2}\right)G(\nu) \tag{19}$$

where $\eta(\tau)$ is the time window. $G(\nu)$ is a frequency window. Compared to the basic WVD kernel, the SPWD kernel acts as a filter of the WVD for the purpose to suppress the cross-term. The SPWD applies window functions independently on both the time and frequency domains of the WVD, which strongly depends on the prior information of the target signal to suppress the cross-terms correctly.

5.2. Application to numerical results

The validation of the present identification procedure is demonstrated through several numerical simulations. The PSW-CWIs with different amplitudes and wavelengths are included in the catenary to perform the numerical simulations.

1) With different amplitudes

Three types of PSW-CWI with a wavelength of 3.3 m and the amplitudes of 0.4 mm, 0.5 mm and 0.6 mm are added to the contact wire. The amplitudes of CWI are slight with respect to the contact wire diameter (which is 6.15 mm) and represent the early wear. The effective range of PSW-CWI is set from 626 m to 643.5 m. The resulting contact forces filtered with the 20 Hz cut-off frequency are presented in Fig. 20(a). The SKs for these three cases are calculated and presented in Fig. 20(b). To facilitate the comparison, the SKs without PSW-CWI are also presented as the benchmark. The deviating wavelengths for these three cases can be identified by searching for the significant increase of SK against its original value. Then EEMD is applied to extract the corresponding IMF containing the deviating wavelength. The extracted IMFs and their spectrums are shown in Fig. 20(c). It is seen that the deviating wavelength of 3.3 m can be observed in the spectrum for each case. The time history of the extracted IMF undergoes a swell in the effective range of the PSW-CWI. Employing the SPWD, the TFR for each case is presented in Fig. 20(d). Looking at the deviating spatial frequency of 0.303 m^{-1}, the energy of the extracted IMF shows a sudden increase in the effective range of the PSW-CWI.

2) With different wavelengths

The PSW-CWI may have the same wavelength components as the contact force, which poses the challenge to identify the deviating wavelength from the contact force. In this section, another wavelength component of the contact force is adopted to represent the dominant wavelength of PSW-CWI. According to the contact force spectrum in Fig. 8, the wavelength of 3.6 m is adopted, and the amplitude is chosen as 0.5 mm. The effective range is set as the same as the above analysis. Though the numerical simulation, the resulting contact forces are presented in Fig. 21(a). The resulting SK as shown in Fig. 21(b) indicates a non-Gaussian behaviour caused by the PSW-CWI at around the specific wavelength. Through EEMD, the corresponding IMF containing the deviating wavelength is extracted. The TFR of the IMF indicates that a PSW-CWI with a spatial frequency of about 0.28 m^{-1} exists at around 630 m in the contact wire. The numerical example demonstrates the validation of the present identification approach for the PSW-CWI with different wavelengths.

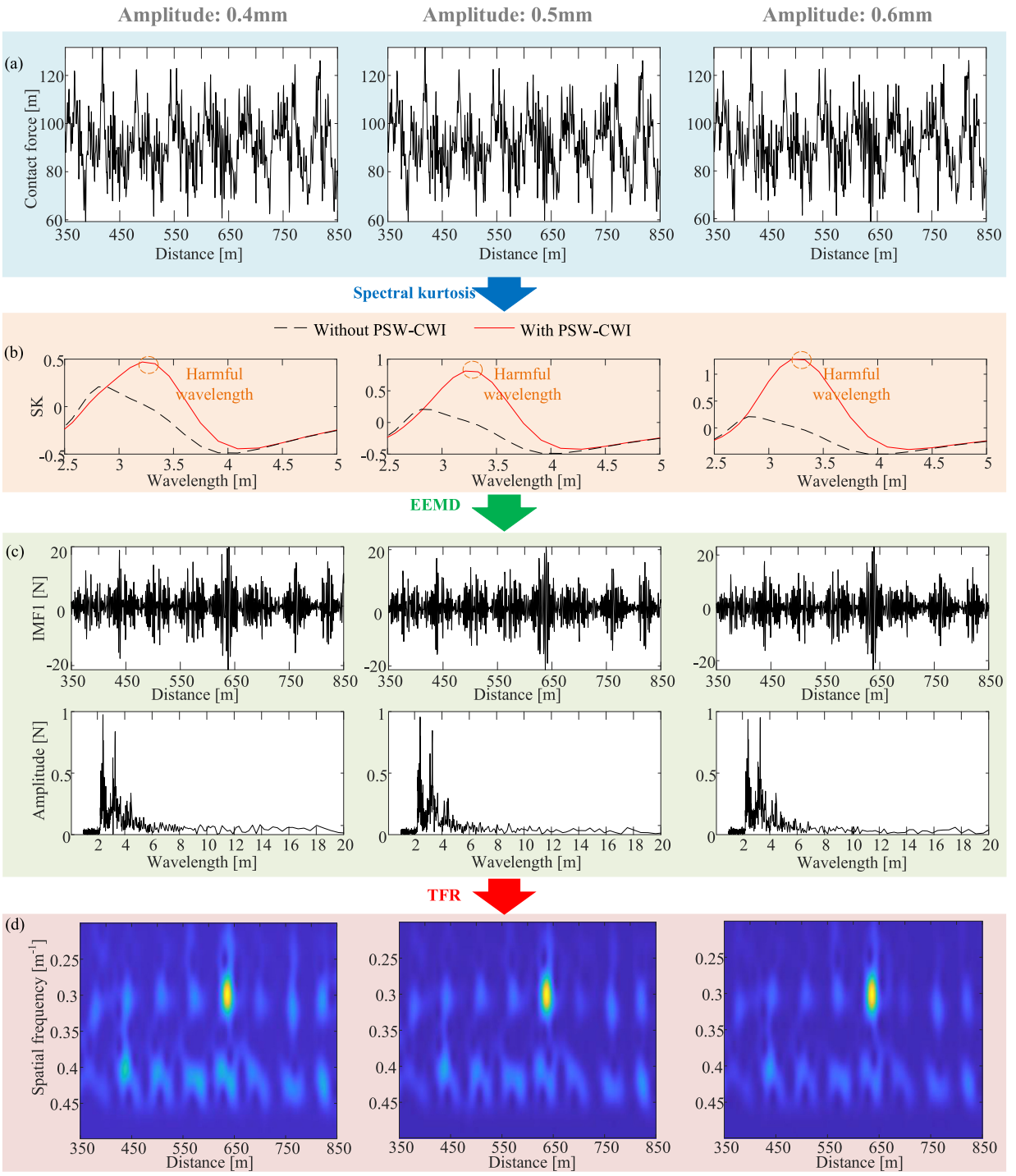

Fig. 20. Identification of PSW-CWI with different amplitudes: a) Resulting contact forces; b) Spectral kurtosis; c) Extracted IMFs containing deviating wavelength and their spectrums; d) Time-frequency representations.

5.3. Application with measurement data

The present identification procedure is implemented using the measurement contact force. Through the above application examples with numerical data, it is seen that the essential part of the identification procedure is to identify the deviating wavelength, which requires a benchmark of SK for comparison. In the numerical simulation, the contact force without PSW-CWI can be taken as the benchmark. In actual operation, the measurement data from multiple inspections can be used to

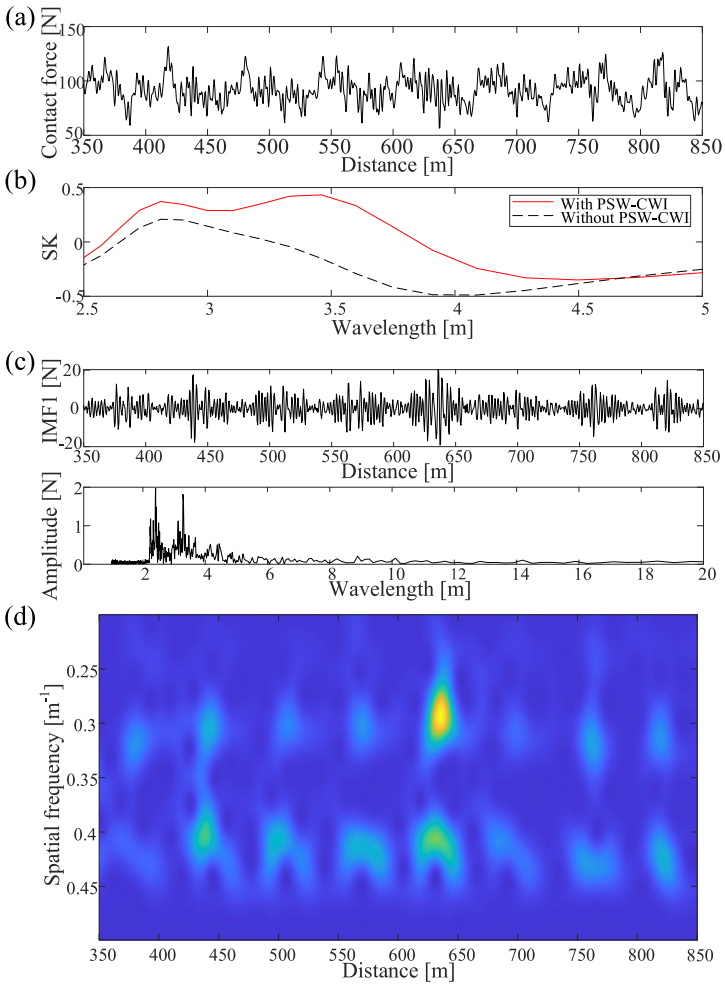

Fig. 21. Identification of PSW-CWI with 3.6 m wavelength: a) Resulting contact forces; b) Spectral kurtosis; c) Extracted IMFs containing deviating wavelength and their spectrums; d) Time-frequency representation.

compare their SKs to identify the deviating wavelength. The contact forces from two times of measurement in Oslo-Eidsvoll railway are presented in Fig. 22(a). Due to the long interval between two measurements, they can describe the catenary health status for different service periods. Through the comparison of their SKs as shown in Fig. 22(b), it is seen that the SK of measurement 2 undergoes a significant increase at the wavelength of 3.23 m, which does not exist in measurement 1. It can be expected that a deviating wavelength may exist in the contact force of measurement 2. The corresponding IMFs containing the deviating wavelength, together with their spectrums, are presented in Fig. 22(c). It is seen that the spectrum of measurement 2 is significantly higher than measurement 1 at around the deviating wavelength. To facilitate the comparison, the TFRs of the IMF of two measurements at the deviating wavelength of 3.23 m are presented in Fig. 22(d). It is seen that several TFR peaks of measurement 2 can be observed. The PSW-CWI with a 3.23 m wavelength is a common wavelength of wear generated in long-term operations. The most serious PSW-CWI appears at around 42.9 km, which deserves special attention in the maintenance following measurement 2.

6. Discussions

According to the above analysis results, some discussions are drawn here.

6.1. Local imperfection

The local imperfection contributes a transient impact to the acceleration. The previous researches mainly used high-frequency acceleration to identify it. The numerical analysis results indicate that the cut-off frequency does not have to reach an extremely high value. It is suggested to increase the cut-off frequency to cover the 1/8 of DD wavelength, in which the effect of local imperfection can be reflected in the panhead acceleration. However, the current measurement acceleration

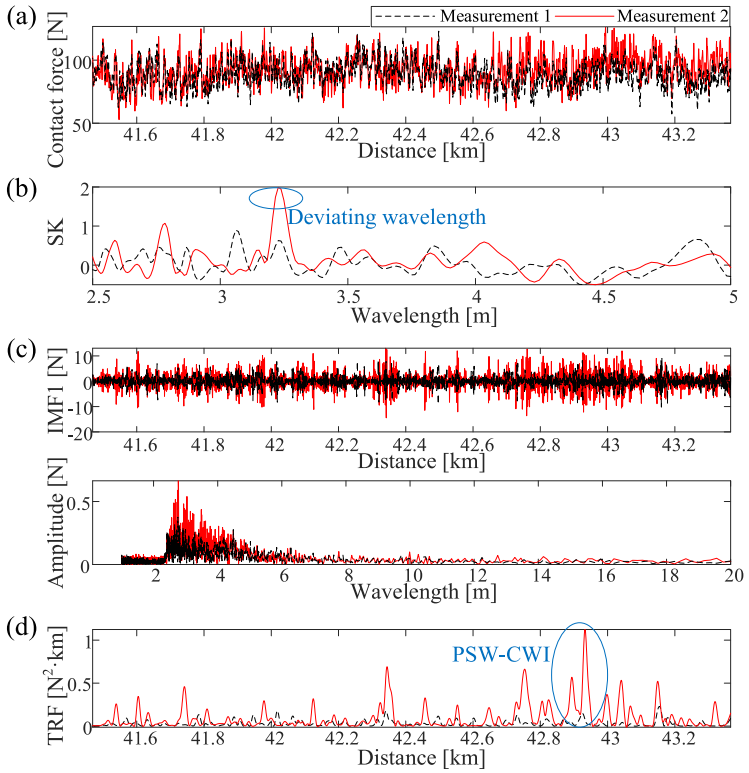

Fig. 22. Identification of PSW-CWI using measurement data: a) Contact forces; b) Spectral kurtosis; c) Extracted IMFs containing deviating wavelength and their spectrums; d) Comparison of TFRs at deviating wavelength.

obtained from the Norwegian railway network can only reflect a part of the 1/4 of DD wavelength. Only some significant imperfections, such as the overlap section, can be identified with the current measurement response. The difference of the identification approach in this work against the previous one [38] is that the EEMD is used to extract the high-order deformation mode which is more sensitive to the transient impact instead of implementing RMS to the original signal. A shortfall of the identification approach can be seen in Fig. 15. The elasticity discontinuity, wave reflection, lumped mass in the contact wire, and even the errors in signal processing can also introduce peaks in the instantaneous energy, which may disturb the identification results. The present method can only give potential positions of local imperfection with a low cut-off frequency. The best solution is to improve the cut-off frequency, which allows for the identification of smaller local imperfections. Another potential solution is to compare multiple measurement results and take the incidental peaks as the suspect local imperfections. The physical meaning of these peaks deserves to be revealed in the future.

6.2. PSW-CWI

The time-frequency analysis method has been proven to effectively capture the PSW-CWI from the contact force [35]. However, the PSW-CWI may have the same wavelength as the contact force. An indicator is desired to identify the deviating wavelength before implementing the time-frequency analysis to localise the PSW-CWI. The above numerical simulation has demonstrated that the SK can be used to indicate the non-Gaussian behaviour caused by the PSW-CWI, which is a potential indicator to determine the deviating wavelength. It can also be seen from Fig. 22 that the measurement data obtained in different service periods show a significant change of the contact force SK at some certain wavelengths. The next step is to collaborate with the maintenance department to validate the identification results.

7. Conclusions

This paper presents potential solutions for identifying two common types of short-wavelength irregularities. The present identification approaches are validated with several numerical examples. The application examples with measurement data indicate that present methods have the potential to be used in actual operation with some improvements in the current monitoring trains. The main conclusions are summarised as follows:

1) The local imperfection can be detected from the panhead acceleration with higher orders of deformable modes. The analysis results indicate that cut-off frequency should be improved to cover the 1/8 of DD wavelength. EEMD is utilised

to extract the IMF containing the DD wavelength. The instantaneous energy of the corresponding IMF obtained by Hilbert transform has the potential to indicate the local imperfection location.

2) The effect of PSW-CWI can be recognised as the introduction of non-Gaussian behaviour into the contact force at specific wavelengths. The SK can be used to indicate the non-Gaussian behaviour and determine the deviating wavelength. The location of the PSW-CWI can be determined by the time-frequency analysis of the IMF containing the identified deviating wavelength. In actual operation, the data from multiple measurements with long-term interval can be compared to identify the deviating wavelength.

Declaration of Competing Interest

The authors declare that they have no known competing financial interests or personal relationships that could have appeared to influence the work reported in this paper.

Acknowledgement

The work presented in this paper is funded by the Norwegian Railway Directorate.

References

[1] W. Zhang, D. Zou, M. Tan, N. Zhou, R. Li, G. Mei, Review of pantograph and catenary interaction, Front. Mech. Eng. (2018), doi:10.1007/s11465-018-0494-x.
[2] EN 50367, EN 50367. Railway applications — current collection systems — technical criteria for the interaction between pantograph and overhead line., 2016.
[3] Y. Song, Z.Z. Liu, A. Ronnquist, P. Navik, Z.Z. Liu, Contact wire irregularity stochastics and effect on high-speed railway pantograph-catenary interactions, IEEE Trans. Instrum. Meas. 69 (2020) 8196–8206, doi:10.1109/TIM.2020.2987457.
[4] H. Wang, Z. Liu, Y. Song, X. Lu, Z. Han, J. Zhang, Y. Wang, Detection of contact wire irregularities using a quadratic time-frequency representation of the pantograph-catenary contact force, IEEE Trans. Instrum. Meas. 65 (2016) 1385–1397, doi:10.1109/TIM.2016.2518879.
[5] H. Chen, B. Jiang, A review of fault detection and diagnosis for the traction system in high-speed trains, IEEE Trans. Intell. Transp. Syst. 21 (2020) 450–465, doi:10.1109/TITS.2019.2897583.
[6] H. Chen, B. Jiang, S.X. Ding, B. Huang, Data-driven fault diagnosis for traction systems in high-speed trains: a survey, challenges, and perspectives, IEEE Trans. Intell. Transp. Syst. (2020), doi:10.1109/tits.2020.3029946.
[7] A. Facchinetti, M. Mauri, Hardware-in-the-loop overhead line emulator for active pantograph testing, IEEE Trans. Ind. Electron. 56 (2009) 4071–4078, doi:10.1109/TIE.2009.2023632.
[8] S. Daocharoenporn, M. Mongkolwongrojn, S. Kulkarni, A.A. Shabana, Prediction of the pantograph/catenary wear using nonlinear multibody system dynamic algorithms, J. Tribol. 141 (2019) 051603, doi:10.1115/1.4042658.
[9] A. Collina, S. Bruni, Numerical simulation of pantograph-overhead equipment interaction, Veh. Syst. Dyn. 38 (2002) 261–291, doi:10.1076/vesd.38.4.261.8286.
[10] Y. Song, Z. Liu, H. Wang, X. Lu, J. Zhang, Nonlinear analysis of wind-induced vibration of high-speed railway catenary and its influence on pantograph–catenary interaction, Veh. Syst. Dyn. 54 (2016) 723–747, doi:10.1080/00423114.2016.1156134.
[11] Y. Song, Z. Liu, F. Duan, Z. Xu, X. Lu, Wave propagation analysis in high-speed railway catenary system subjected to a moving pantograph, Appl. Math. Model. 59 (2018) 20–38, doi:10.1016/j.apm.2018.01.001.
[12] J. Gil, S. Gregori, M. Tur, F.J. Fuenmayor, Analytical model of the pantograph–catenary dynamic interaction and comparison with numerical simulations, Veh. Syst. Dyn. (2020) 1–24, doi:10.1080/00423114.2020.1802493.
[13] A. Bautista, J. Montesinos, P. Pintado, Dynamic interaction between pantograph and rigid overhead lines using a coupled FEM - multibody procedure, Mech. Mach. Theory. 97 (2016) 100–111, doi:10.1016/j.mechmachtheory.2015.10.009.
[14] J. Pombo, J. Ambrósio, Influence of pantograph suspension characteristics on the contact quality with the catenary for high speed trains, Comput. Struct. 110–111 (2012) 32–42, doi:10.1016/j.compstruc.2012.06.005.
[15] J.H. Seo, H. Sugiyama, A.A. Shabana, Three-dimensional large deformation analysis of the multibody pantograph/catenary systems, Nonlinear Dyn. 42 (2005) 199–215, doi:10.1007/s11071-005-2789-9.
[16] P. Zdziebko, A. Martowicz, T. Uhl, An investigation on the active control strategy for a high-speed pantograph using co-simulations, Proc. Inst. Mech. Eng. Part I J. Syst. Control Eng. 233 (2019) 370–383, doi:10.1177/0959651818783645.
[17] C.M. Pappalardo, M.D. Patel, B. Tinsley, A.A. Shabana, Contact force control In multibody pantograph/catenary systems, Proc. Inst. Mech. Eng. Part K J. Multi-Body Dyn. (2016), doi:10.1177/1464419315604756.
[18] J. Pombo, J. Ambrosio, M. Pereira, F. Rauter, A. Collina, A. Facchinetti, Influence of the aerodynamic forces on the pantograph-catenary system for high-speed trains, Veh. Syst. Dyn. 47 (2009) 1327–1347, doi:10.1080/00423110802613402.
[19] M. Zhang, F. Xu, O. Øiseth, Aerodynamic damping models for vortex-induced vibration of a rectangular 4:1 cylinder: comparison of modeling schemes, J. Wind Eng. Ind. Aerodyn. 205 (2020), doi:10.1016/j.jweia.2020.104321.
[20] M. Zhang, F. Xu, Y. Han, Assessment of wind-induced nonlinear post-critical performance of bridge decks, J. Wind Eng. Ind. Aerodyn. 203 (2020), doi:10.1016/j.jweia.2020.104251.
[21] Y. Song, Z. Liu, F. Duan, X. Lu, H. Wang, Study on wind-induced vibration behavior of railway catenary in spatial stochastic wind field based on nonlinear finite element procedure, J. Vib. Acoust. Trans. ASME 140 (2018) 011010-1–14, doi:10.1115/1.4037521.
[22] Y. Song, M. Zhang, H. Wang, A response spectrum analysis of wind deflection in railway overhead contact lines using pseudo-excitation method, IEEE Trans. Veh. Technol. (2021) 1 –1, doi:10.1109/tvt.2021.3054459.
[23] Y. Song, Z. Liu, H. Wang, J. Zhang, X. Lu, F. Duan, Analysis of the galloping behaviour of an electrified railway overhead contact line using the non-linear finite element method, Proc. Inst. Mech. Eng. Part F J. Rail Rapid Transit. 232 (2018) 2339–2352, doi:10.1177/0954409718769751.
[24] Z. Wang, P. Allen, G. Mei, R. Wang, Z. Yin, W. Zhang, Influence of wheel-polygonal wear on the dynamic forces within the axle-box bearing of a high-speed train, Veh. Syst. Dyn. 58 (2020) 1385–1406, doi:10.1080/00423114.2019.1626013.
[25] Z. Wang, G. Mei, Q. Xiong, Z. Yin, W. Zhang, Motor car–track spatial coupled dynamics model of a high-speed train with traction transmission systems, Mech. Mach. Theory. 137 (2019) 386–403, doi:10.1016/j.mechmachtheory.2019.03.032.
[26] Y. Song, Z. Wang, Z. Liu, R. Wang, A spatial coupling model to study dynamic performance of pantograph-catenary with vehicle-track excitation, Mech. Syst. Signal Process. 151 (2021) 107336, doi:10.1016/j.ymssp.2020.107336.
[27] Z. Xu, Y. Song, Z. Liu, Effective measures to improve current collection quality for double pantographs and catenary based on wave propagation analysis, IEEE Trans. Veh. Technol. 69 (2020) 6299–6309, doi:10.1109/TVT.2020.2985382.
[28] Z. Liu, P.A. Jönsson, S. Stichel, A. Rønnquist, On the implementation of an auxiliary pantograph for speed increase on existing lines, Veh. Syst. Dyn. 54 (2016) 1077–1097, doi:10.1080/00423114.2016.1187278.

[29] Y. Song, Z. Liu, X. Lu, Dynamic performance of high-speed railway overhead contact line interacting with pantograph considering local dropper defect, IEEE Trans. Veh. Technol. 69 (2020) 5958–5967, doi:10.1109/TVT.2020.2984060.
[30] F. Vesali, M.A. Rezvani, H. Molatefi, M. Hecht, Static form-finding of normal and defective catenaries based on the analytical exact solution of the tensile Euler–Bernoulli beam, Proc. Inst. Mech. Eng. Part F J. Rail Rapid Transit. 233 (2019) 691–700, doi:10.1177/0954409718808990.
[31] P. Nåvik, S. Derosa, A. Rønnquist, Development of an index for quantification of structural dynamic response in a railway catenary section, Eng. Struct. 222 (2020) 111154, doi:10.1016/j.engstruct.2020.111154.
[32] T. Jiang, G.T. Frøseth, A. Rønnquist, E. Fagerholt, A robust line-tracking photogrammetry method for uplift measurements of railway catenary systems in noisy backgrounds, Mech. Syst. Signal Process. 144 (2020), doi:10.1016/j.ymssp.2020.106888.
[33] W. Liu, Z. Liu, Q. Li, Z. Han, A. Nunez, High-precision detection method for structure parameters of catenary cantilever devices using 3D point cloud data, IEEE Trans. Instrum. Meas. (2020) 1 –1, doi:10.1109/tim.2020.3045801.
[34] Y. Song, P. Antunes, J. Pombo, Z. Liu, A methodology to study high-speed pantograph-catenary interaction with realistic contact wire irregularities, Mech. Mach. Theory 152 (2020) 103940, doi:10.1016/j.mechmachtheory.2020.103940.
[35] H. Wang, A. Núñez, Z. Liu, Y. Song, F. Duan, R. Dollevoet, Analysis of the evolvement of contact wire wear irregularity in railway catenary based on historical data, Veh. Syst. Dyn. 56 (2018) 1207–1232, doi:10.1080/00423114.2017.1408919.
[36] H. Wang, Z. Liu, A. Núñez, R. Dollevoet, Entropy-based local irregularity detection for high-speed railway catenaries with frequent inspections, IEEE Trans. Instrum. Meas. 68 (2019) 3536–3547, doi:10.1109/TIM.2018.2881529.
[37] Y. Song, A. Rønnquist, P. Nåvik, Assessment of the high-frequency response in railway pantograph-catenary interaction based on numerical simulation, IEEE Trans. Veh. Technol. 69 (2020) 10596–10605, doi:10.1109/TVT.2020.3015044.
[38] M. Carnevale, A. Collina, Processing of collector acceleration data for condition-based monitoring of overhead lines, Proc. Inst. Mech. Eng. Part F J. Rail Rapid Transit. 230 (2016) 472–485, doi:10.1177/0954409714545637.
[39] A.A. Shabana, K.E. Zaazaa, H. Sugiyama, Railroad Vehicle Dynamics, CRC Press, 2007, doi:10.1201/9781420045857.
[40] J. Antoni, The spectral kurtosis: a useful tool for characterising non-stationary signals, Mech. Syst. Signal Process. 20 (2006) 282–307, doi:10.1016/j.ymssp.2004.09.001.
[41] Y. Song, Z. Liu, Z. Xu, J. Zhang, Developed moving mesh method for high-speed railway pantograph-catenary interaction based on nonlinear finite element procedure, Int. J. Rail Transp. 7 (2019) 173–190, doi:10.1080/23248378.2018.1532330.
[42] S. Bruni, J. Ambrosio, A. Carnicero, Y.H. Cho, L. Finner, M. Ikeda, S.Y. Kwon, J.P. Massat, S. Stichel, M. Tur, W. Zhang, The results of the pantograph-catenary interaction benchmark, Veh. Syst. Dyn. 53 (2015) 412–435, doi:10.1080/00423114.2014.953183.
[43] W. Soboyejo, Mechanical Properties of Engineered Materials, 2002 CRC Press, doi:10.1201/9780203910399.
[44] M. Carnevale, A. Facchinetti, L. Maggiori, D. Rocchi, Computational fluid dynamics as a means of assessing the influence of aerodynamic forces on the mean contact force acting on a pantograph, Proc. Inst. Mech. Eng. Part F J. Rail Rapid Transit. 230 (2016) 1698–1713, doi:10.1177/0954409715606748.
[45] M. Carnevale, A. Facchinetti, D. Rocchi, Procedure to assess the role of railway pantograph components in generating the aerodynamic uplift, J. Wind Eng. Ind. Aerodyn. 160 (2017) 16–29, doi:10.1016/j.jweia.2016.11.003.
[46] BSIBS EN 50317: Railway Applications - Current Collection Systems - Requirements for and Validation of Measurements of the Dynamic Interaction Between Pantograph and Overhead Contact Line, European Standards (EN), Brussels, 2012.
[47] A. Collina, A. Lo Conte, M. Carnevale, Effect of collector deformable modes in pantograph-catenary dynamic interaction, Proc. Inst. Mech. Eng. Part F J. Rail Rapid Transit. 223 (2009) 1–14, doi:10.1243/09544097JRRT212.
[48] B. Chen, P. Yin, Y. Gao, F. Peng, Use of the correlated EEMD and time-spectral kurtosis for bearing defect detection under large speed variation, Mech. Mach. Theory. 129 (2018) 162–174, doi:10.1016/j.mechmachtheory.2018.07.017.
[49] D. Yang, Y. Liu, S. Li, X. Li, L. Ma, Gear fault diagnosis based on support vector machine optimized by artificial bee colony algorithm, Mech. Mach. Theory. 90 (2015) 219–229, doi:10.1016/j.mechmachtheory.2015.03.013.
[50] Z. Wu, N.E. Huang, Ensemble empirical mode decomposition: a noise-assisted data analysis method, Adv. Adapt. Data Anal. 1 (2009) 1–41, doi:10.1142/S1793536909000047.
[51] L. Cohen, Generalized phase-space distribution functions, J. Math. Phys. 7 (1966) 781–786, doi:10.1063/1.1931206.